# Broad frequency tidal dynamics simulated by a high-resolution global ocean tide model forced by ephemerides

P. Weis,[1,2,3] M. Thomas,[4] and J. Sündermann[1]

Received 17 September 2007; revised 21 July 2008; accepted 18 August 2008; published 30 October 2008.

[1] Traditionally, global ocean tide models are forced by individual partial tides resulting from a decomposition of the complete lunisolar tidal potential in Fourier components. Implicitly, this approach neglects nonlinear interactions between partial tides. This can be partly compensated by a superposition of a selection of partial tides. In order to ensure the full dynamics, the Tidal Model forced by Ephemerides (TiME) incorporates the tidal potential of second degree calculated online from analytical ephemerides and utilizes the classical shallow-water equations with a horizontal resolution of 5 min globally. Interactions between partial tides generate shallow-water tides which are shown to form in extended shelf areas where they develop the highest amplitudes. However, as they propagate into the open ocean, they should be regarded as a global phenomenon. Simulations with TiME confirm that $M_4$ is particularly pronounced in the Atlantic and suggest further areas of strong energy fluxes in the southern Pacific. $MN_4$ is strongest in the Atlantic and $MS_4$, $2SM_2$, and $MK_3$ mainly spread out into the Indian Ocean.

**Citation:** Weis, P., M. Thomas, and J. Sündermann (2008), Broad frequency tidal dynamics simulated by a high-resolution global ocean tide model forced by ephemerides, *J. Geophys. Res.*, *113*, C10029, doi:10.1029/2007JC004556.

## 1. Introduction

[2] As measurements of the sea surface elevation have become more abundant in recent years, most developments of ocean tide models have been conducted by assimilating data [e.g., *Egbert et al.*, 1994; *Zahel*, 1995; *Lefèvre et al.*, 2002]. The predictions of the sea surface elevation due to ocean tides have been improved dramatically with this approach [*Shum et al.*, 1997]. Along with the presentation of the newest set of tidal atlases calculated with the data assimilating FES model, *Lyard et al.* [2006] indicate that the current modeling approach has reached an upper limit of accuracy, calling for new techniques and approaches.

[3] One of the reasons is the necessity to adequately consider the abundant nonlinearities in the global tidal dynamics. *Lyard et al.* [2006] already present a global chart of sea surface elevations of the nonlinear overtide $M_4$, a higher harmonic of the $M_2$-tide, predicting comparatively high $M_4$ amplitudes for the Atlantic Ocean. *Andersen et al.* [2006] investigated the $M_4$-tide on the Northwestern European Shelf, where it reaches substantial amplitudes, considering the Lyard et al. atlas and satellite data. *Ray* [2007] studied its propagation in the deep waters of the Atlantic Ocean by analyzing data from Topex/Poseidon and Jason-1 unraveling some conspicuous patterns like a near-standing wave in the Gulf of Guinea and an anomalous increase in energy flux off the Northwestern African coast and confirming the significance of $M_4$ in the open ocean.

[4] Among further approaches in global ocean tide modeling was the forcing of a general circulation model with the full lunisolar tidal potential rather than just single or a suite of dominating partial tides [e.g., *Thomas*, 2001; *Thomas et al.*, 2001]. This model allows for interactions of tidal currents with other ocean currents and rather aims at large-scale phenomena and, because of its relatively coarse model resolution, does not fully capture small-scale nonlinearities.

[5] The objective of the present study was to develop a high-resolution, unconstrained time-stepping ocean model allowing for investigations of nonlinear interactions within global ocean tide dynamics as pure and complete as possible. The model is forced by the complete lunisolar tidal potential of second degree derived from the positions of moon and sun (ephemerides) and applies the classical nonlinear shallow-water equations. This leads to real-time simulations. As ocean tides strongly depend on the topography of the oceans, the model resolution has been chosen to be constant $1/12^\circ$ ($5'$) in longitude and latitude which is as high as is currently computationally feasible. The actual distance between two grid points ranges from 2 to 10 km. The model also includes the Arctic Ocean which is often neglected in other model approaches.

[6] This particular setup enables the description of nonlinearities in ocean tide dynamics and the formation of shallow-water tides due to interactions between partial tides. The novel approach with the forcing by the

[1]Institute of Oceanography, University of Hamburg, Hamburg, Germany.
[2]International Max Planck Research School on Earth System Modelling, Hamburg, Germany.
[3]Now at Institute of Isotope Geochemistry and Mineral Resources, ETH Zurich, Zurich, Switzerland.
[4]Geodesy and Remote Sensing, GeoForschungsZentrum, Potsdam, Germany.


0148-0227/08/2007JC004556

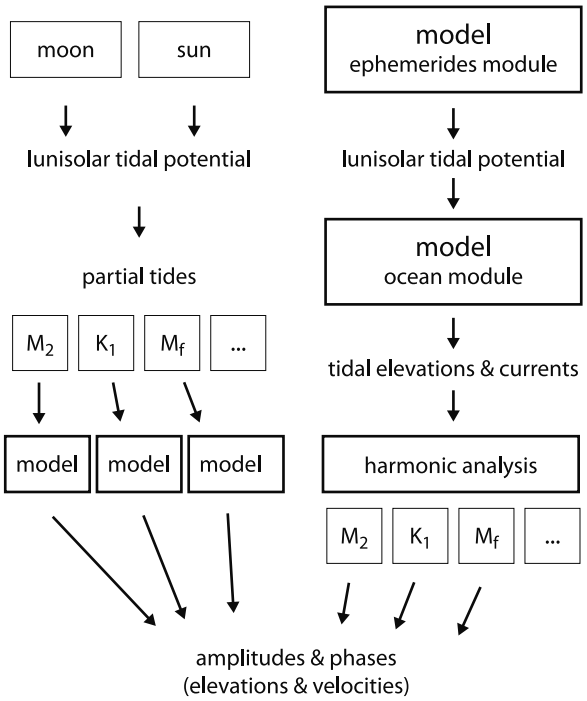


**Figure 1.** Flow diagram of the two optional setups of TiME. The left path represents the classical partial tide forcing. The right path is the novel approach of the complete forcing with subsequent harmonic analysis.

complete lunisolar tidal potential presented in this study includes all partial tides simultaneously. The nonlinear terms of the model equations are most influential in shallow waters which are resolved by the model due to its high spatial resolution.

[7] The interest in shallow-water tides has a long history in oceanography and has recently been reviewed by *Andersen et al.* [2006]. However, due to limitations in computational resources modeling studies have mostly focused on regional shelf-areas. The most studied region is the Northwestern European Shelf [e.g., *Davies et al.*, 1997; *Kwong et al.*, 1997; *Andersen*, 1999] followed by the Patagonian Shelf [e.g., *Glorioso and Flather*, 1997]. In regional tidal modeling sea surface elevations and tidal currents at the model domain boundaries have to be prescribed. This is particularly challenging for the nonlinear constituents because, so far, there were hardly any measurements in the open ocean and global numerical models prescribing these constituents. In a global modeling approach, this becomes unnecessary.

[8] Although shallow-water tides mainly form in relatively restricted areas, they still contribute to the global tidal oscillation system: (1) from their place of origin they are known to propagate into the open ocean and (2) in extended shelf regions they strongly influence the main astronomical tides.

[9] We consider it worth investigating how the classical nonlinear shallow-water equations describe the ocean tides in the combination of globally high-resolution with full forcing. In this respect, the model is the first of its kind. However, predictions of tidal elevations and currents of the main astronomical tides will not be comparable to the accuracy of current models either assimilating data or utilizing parameterizations derived from data assimilation models.

## 2. The Model Approach TiME

[10] The Tidal Model forced by Ephemerides (TiME) consists of a vertically integrated barotropic ocean module (section 2.1) which is forced by an astronomic module calculating the gravitational potential (section 2.2) and accompanied by a geodetic module calculating instantaneous angular momentum budgets (not described here). TiME can be run with the user's choice of either a single selected partial tide or the complete lunisolar tidal potential derived from analytical ephemerides calculated online (Figure 1). This second option represents "real-time" simulations.

[11] Until now, most research on ocean tides has been done using partial tide forcing - either with a single one or a suite of the main partial tides. Thus the results of simulations utilizing the complete forcing have to be post-processed so that the results are comparable with the results from other studies. The amplitude and phase values of selected partial tides are derived from the time series of the real-time simulations through a harmonic analysis (section 2.3).

[12] For the traditional forcing (Figure 1, left path), the lunisolar tidal potential is divided into partial tides, each one describing a certain aspect of the orbits of moon or earth. They are defined by their respective astronomic arguments or Doodson coefficients which describe the frequency of each partial tide. The resulting elevations and velocities are attributed to the period of the specific partial tide and can be represented by amplitude and phase values.

[13] The path on the right-hand side of Figure 1 characterizes the novel approach with complete forcing which is the focus of this study. With the newly implemented ephemerides module, the model calculates the position of the tide-generating bodies, the moon and sun, determines their complete tidal potential of second degree and uses this total forcing to drive the ocean module of TiME. By extracting the frequencies of certain partial tides from these time series through a harmonic analysis, the results of the real-time forcing can be transferred from the time-domain to the frequency-domain.

### 2.1. Ocean Module

[14] The main part of TiME is a barotropic ocean model based on the Navier-Stokes equations. The equations of motion and continuity define the horizontal velocity vector $\mathbf{v} = (u, v)$ and the sea surface elevation $\zeta$ as used by *Zahel* [1977] and *Seiler* [1991]:

$$\frac{\partial \mathbf{v}}{\partial t} + (\mathbf{v} \cdot \nabla)\mathbf{v} = \gamma \nabla \Phi - \mathbf{f} \times \mathbf{v} - g' \nabla \zeta - \mathbf{B} + \mathbf{R} \qquad (1)$$

$$\frac{\partial \zeta}{\partial t} = -\nabla \cdot (H\mathbf{v}). \qquad (2)$$

where $\mathbf{f} = 2\boldsymbol{\Omega}$ sin $\phi$ is the Coriolis parameter with the mean angular velocity of the earth $\boldsymbol{\Omega}$ and $\phi$ the geographical

latitude. The tidal forcing $\nabla\Phi$ is calculated by the astronomic module of TiME and will be discussed in section 2.2. The influence of the tidal deformation of the solid earth on the oceanic tidal potential is taken into account and defined by the Love numbers with the factor $\gamma = 1 + k_2 - h_2 = 0.69$.

[15] The effect of load and self-attraction of water masses is taken into account in a parameterized form [*Accad and Pekeris*, 1978] defined as $\Phi_{LSA} = g\epsilon\zeta$, eventually leading to the "reduced gravity" $g' = (1 - \epsilon)\, g$ referring to the gravitational acceleration $g$. Values of $\epsilon$ are in the range of about 0.08 to 0.12 [*Parke*, 1982].

[16] The quadratic bottom friction **B** and the prescription of turbulent effects via the eddy-viscosity term **R** are described by

$$\mathbf{B} = \mathbf{v}\,\frac{r}{H}\,\sqrt{u^2 + v^2} \tag{3}$$

$$\mathbf{R} = \frac{A_H}{a^2}\left[\frac{\partial^2 \mathbf{v}}{\cos\phi\,\partial\lambda^2} + \frac{\partial^2 \mathbf{v}}{\partial\phi^2} - \tan\phi\frac{\partial \mathbf{v}}{\partial\phi} - \left(1 + \tan^2\phi\right)\mathbf{v} + 2\tan\phi\frac{\partial \mathbf{v}}{\partial\lambda}\right] \tag{4}$$

and include the bottom friction coefficient $r = 3 \cdot 10^{-3}$, the water depth $H = d + \zeta$ ($d$ being the undisturbed depth), the mean radius of the earth $a$, and the eddy-viscosity coefficient $A_H$ which depends on the horizontal resolution and lies in the order of magnitude of $10^{-3}$ to $10^{-5}$ m$^2$ s$^{-1}$ (see *Weis* [2006] for details).

[17] Nonlinearities are mainly captured by the continuity equation (wave drift term) and the advection term $(\mathbf{v} \cdot \nabla)\,\mathbf{v}$ and the quadratic bottom friction **B** in the equation of motion [see, e.g., *Parker*, 1991; *Le Provost*, 1991].

[18] The ocean module was taken in large parts from the partial tide model of *Seiler* [1989] which is based on the equations of *Zahel* [1977] and utilizes a semi-implicit algorithm as described by *Backhaus* [1983]. The resolution has been changed from the original one degree [*Seiler*, 1989] to a series of higher resolving versions. The user can now choose between resolutions of 20, 15, 10, or 5 min based on either the GEBCO [*IOC et al.*, 2003] or ETOPO topographies [*NOAA*, 1988]. Although the simulations for this study have been performed on the high-performance computer of the DKRZ (Deutsches Klimarechenzentrum) the 5′ resolution version of TiME is still at the upper limit of manageable run times. One simulated calendar year currently requires about 180 hours of CPU time.

[19] The equations of *Seiler* [1989] were reformulated in a slightly different semi-implicit numerical scheme [*Backhaus*, 1985] which has been shown to be less dependent on the chosen modeling time-step. A two-step pole-ward zonal resolution change has been implemented because convergence used to be slowest toward the North Pole and because the smallest actual mesh size of the modeling grid constrains the largest possible modeling time-step (see *Weis* [2006] for details). The 5′ resolution version of TiME currently applies a time-step of 5 min.

### 2.2. Astronomic Module

[20] Ocean tides develop due to the gravitational forces of the moon and sun and can be formulated as the second degree astronomic tidal potential $V_2$ [*Bartels*, 1957]:

$$V_2 = G(a) \cdot \left(\frac{c}{R}\right)^3 \cdot \left[\left(1 - 3\sin^2\delta\right)\left(1 - 3\cos^2\phi\right) - \sin(2\phi)\sin(2\delta)\cos\tau + \cos^2\phi\cos^2\delta\cos(2\tau)\right] \tag{5}$$

where $G(a)$ is the gravitational constant, $a$ the mean radius of the earth, $R$ the geocentric distance, $c$ the greater half axis of the orbit, and $\delta$ the declination of the tide-generating body. The local hour angle $\tau$ is related to the right ascension $\alpha$ of the respective celestial body through $\tau = T_{sid} - \alpha$ with the local sidereal time $T_{sid}$.

[21] The three terms of equation (5) represent different groups of spherical harmonics and define the tidal bands: (1) the zonal term reflecting the long-period tides, e.g., fortnightly, monthly, and annual; (2) the tesseral term describing the band of diurnal tidal constituents; and (3) the sectorial term composing the semi-diurnal tides.

[22] Each of the three tidal bands from equation (5) can be broken up into partial tides, the traditional way of forcing an ocean tide model. The main advantage of using partial tides is to deal with exactly known and fixed periods. Once the ocean tide model has adjusted to the strictly periodically acting force, e.g., the $M_2$-tide, the system will respond in the exact same way every subsequent period. It is straightforward to perform such simulations and the analyses. In remote sensing and field campaigns, the fixed periods allow the extraction of partial tides from collected series of sea surface elevation measurements.

[23] For the new real-time approach, equation (5) is incorporated directly. To this end, the positions of the moon and sun with respect to the center of the earth have to be known. The module for the complete lunisolar forcing utilized in TiME has been taken from *Thomas* [2001] and *Hellmich* [2003] where a detailed description of the theory, the computational calculations and a thorough validation of the module are provided.

[24] The module independently describes the orbits of both the moon and earth according to an algorithm based on fundamental angles. *Hellmich* [2003] discusses the advantages of this algorithm compared with an alternative one based on Kepler's orbital elements by evaluating the results with the data set DE200 of numerical ephemerides provided by the Jet Propulsion Laboratory (JPL). With the ephemerides module independently calculating the instantaneous values of declination, right ascension and actual distance for both the moon and sun the complete tidal forcing on any point on the globe can be calculated for every modeling time-step.

[25] The advantage of the full forcing is that all partial tides from the second degree tidal potential are included simultaneously and thus represent the complete dynamics. This also allows for nonlinear interactions between partial tides which leads to the formation of shallow-water tides.

**Table 1.** Partial Tides Extracted From Real-Time Simulations[a]

| Astronomic Tides | | | | | | Shallow-Water Tides | |
|---|---|---|---|---|---|---|---|
| Long-Period | | Diurnal | | Semi-Diurnal | | Semi- to Eighth-Diurnal | |
| Tide | $\sigma_{pt}$ | Tide | $\sigma_{pt}$ | Tide | $\sigma_{pt}$ | Tide | $\sigma_{pt}$ |
| *Sa* | 0.041067 | $Q_1$ | 13.398661 | $2N_2$ | 27.895355 | $2SM_2$ | 31.015896 |
| *Ssa* | 0.082137 | $O_1$ | 13.943036 | $\mu_2$ | 27.968208 | $MO_3$ | 42.927140 |
| *MSm* | 0.471521 | $P_1$ | 14.958931 | $N_2$ | 28.439730 | $SO_3$ | 43.943036 |
| *Mm* | 0.544375 | $K_1$ | 15.041069 | $M_2$ | 28.984104 | $MK_3$ | 44.025173 |
| *MSf* | 1.015896 | | | $L_2$ | 29.528479 | $MN_4$ | 57.423834 |
| *Mf* | 1.098033 | | | $T_2$ | 29.958933 | $M_4$ | 57.968208 |
| | | | | $S_2$ | 30.000000 | $MS_4$ | 58.984104 |
| | | | | $K_2$ | 30.082137 | $MK_4$ | 59.066242 |
| | | | | $\eta_2$ | 30.626512 | $M_6$ | 86.952313 |
| | | | | | | $2MS_6$ | 87.968208 |
| | | | | | | $2MK_6$ | 88.050346 |
| | | | | | | $M_8$ | 115.936417 |
| | | | | | | $3MS_8$ | 116.952313 |
| | | | | | | $3MK_8$ | 117.034450 |

[a]Frequency in degrees/hour.

### 2.3. Harmonic Analysis and Setup

[26] The results of experiments with the complete lunisolar tidal potential are real-time values and do not form fixed periods such as is the case for the partial tide simulations. However, the frequencies included in the time series of the sea surface elevations and ocean currents can be derived from the astronomic tidal potential. Therefore, in the special case of ocean tides, the classical Fourier analysis can be replaced by a harmonic analysis with a discrete number of well-defined partial tide frequencies. To this end, the time series to be analyzed can be regarded as having the form [*Emery and Thompson*, 1998]

$$x(t_n) = \bar{x} + \sum_{pt=1}^{M} \left[ A_{pt} \cos\left(2\pi\sigma_{pt} t_n\right) + B_{pt} \sin\left(2\pi\sigma_{pt} t_n\right) \right] + x_r(t_n) \tag{6}$$

where $\sigma_{pt}$ is the respective tidal frequency, $\bar{x}$ the mean value of the record and $x_r(t_n)$ the residual time series. $A_{pt}$ and $B_{pt}$ define the respective amplitude ($C_{pt} = \sqrt{A_{pt}^2 + B_{pt}^2}$) and phase values ($\phi_{pt} = \tan^{-1}(B_{pt}/A_{pt})$).

[27] The selection of determinable partial tides depends on two criteria: the relative significance of the given tide and the resolvability of two "neighboring" frequencies. Considering a time-step of one hour, the resolvability is determined by the length of the time series $T$ with the criterion $T > \dfrac{1}{|\sigma_{pt_1} - \sigma_{pt_2}|}$ [*Emery and Thompson*, 1998].

[28] The two predominant partial tides $M_2$ and $S_2$, for example, can be unambiguously distinguished with a time series of 14.7 days. The longer the time series the more constituents can be resolved, including long-period tides.

[29] The frequencies of shallow-water tides can be determined by adding or subtracting the astronomical arguments of the partial tides involved and, consequently, they can be included in the harmonic analysis. The most significant ones are the fourth-diurnal compound tides which result from the addition of two semi-diurnal tides, e.g., the $MS_4$-tide results from interactions of $M_2 + S_2$. The interaction of the $M_2$ with itself results in the special case of a compound tide, the overtide $M_4$.

[30] Experiments conducted for this study demonstrated that all partial tides listed by *Bartels* [1957] (including the solar annual tide *Sa*) should be unambiguously distinguishable with a time series of at least 366 days. For this study, time series of 400 days length with a sampling interval of 30 min were recorded from each simulation (5′, 10′, 15′, and 20′ spatial resolution) after an initial spin-up of 150 days.

[31] The analyses contained the entire global fields of sea surface elevation and currents. For simulations performed with the 5-min resolution, this means more than 6 Mio wet points for the three variables $\zeta$, $u$, and $v$. As the computational time of the harmonic analysis increases with the square of the number of constituents [*Emery and Thompson*, 1998], only a selection of primary astronomic partial tides and the most significant compound and overtides has been included (Table 1).

[32] In order to account for the modulation of the moon's 18.6 year nodal cycle, nodal corrections have been performed for all lunar partial tides extracted. This modulation adds the time-dependent amplitude and phase corrections $j(t)$ and $v(t)$ to the solution resulting in $j(t) \cdot C_{pt}\cos(\sigma_{pt}t + v(t) - \Phi_{pt})$. For relatively short time series of about one year, a valid approximation of $j(t)$ and $v(t)$ is taking the values at the middle of the time series and regarding them as constant $j$ and $v$ for every partial tide, respectively [*Horn*, 1967; *Pugh*, 1987; *Foreman and Henry*, 1989].

## 3. Evaluation of Model Results

[33] From the results of simulations with the complete lunisolar tidal potential, all 13 partial tides considered in the MEOM data set [*Le Provost*, 1995] have been determined through harmonic analysis and verified by means of the pelagic data set. Simulations of five partial tides have been performed ($M_2$, $S_2$, $N_2$, $O_1$, and $P_1$) with the traditional forcing and will serve as "reference runs".

[34] Table 2 shows root-mean-square (rms) differences calculated as

$$rms = \sqrt{\frac{1}{2N} \cdot \left[ \sum_{n=1}^{N} \left( A_n^a \cos\phi_n^a - A_n^b \cos\phi_n^b \right)^2 + \sum_{n=1}^{N} \left( A_n^a \sin\phi_n^a - A_n^b \sin\phi_n^b \right)^2 \right]} \tag{7}$$

with $A_n$ and $\phi_n$ being the amplitude and phase values of the respective tide at location $n$ and $a$ and $b$ referring to the compared data sets. As a general trend the rms values have been improved by the increase of the model resolution from 10′ to 5′, albeit by maximal 2 cm in case of the $M_2$, with the exception of the $K_2$ and $O_1$. In comparison with the results of 5′ resolution simulation with single partial tide forcing, only rms values of $S_2$ and $P_1$ show an improvement with the new approach while $M_2$, $N_2$ and $O_1$ seem to be slightly better captured by the traditional forcing approach.

**Table 2.** Global rms Differences (in cm) in Comparison With ST103

| Tide | Full (5′) | Full (10′) | Partial (5′) |
|---|---|---|---|
| $2N_2$ | 0.46 | 0.56 | |
| $\mu_2$ | 0.62 | 0.69 | |
| $N_2$ | 3.53 | 3.97 | 3.08 |
| $\nu_2$ | 0.63 | 0.74 | |
| $M_2$ | 20.49 | 22.85 | 20.12 |
| $L_2$ | 0.48 | 0.70 | |
| $T_2$ | 0.43 | 0.47 | |
| $S_2$ | 7.34 | 7.92 | 8.05 |
| $K_2$ | 2.01 | 1.82 | |
| $Q_1$ | 1.11 | 1.14 | |
| $O_1$ | 5.89 | 5.30 | 4.43 |
| $P_1$ | 1.09 | 1.30 | 1.13 |
| $K_1$ | 3.53 | 4.30 | |

[35] Compared to other modeling approaches the rms values are relatively high as data assimilation models normally report rms values of a few centimeters, even for the $M_2$ tide [e.g., *Lyard et al.*, 2006]. In order to further investigate the reason for the rms values of Table 2, we performed a complex linear regression [*Hufschmidt*, 1995; *Thomas and Sündermann*, 1999]. To this end, the sea surface elevations are considered complex-valued as $\zeta_{pt} = A_{pt} \cdot e^{i \cdot \sigma_{pt} \cdot t \cdot e - i \cdot \phi_{pt}}$ with $i = \sqrt{-1}$ and $pt$ referring to the respective partial tide. The correlation coefficient is defined as

$$r_{ab} = \sqrt{\frac{\left| \sum_{n=1}^{N} \left[ \left( \zeta_n^a - \overline{\zeta}_n^a \right) \cdot \left( \zeta_n^b - \overline{\zeta}_n^b \right) \right] \right|^2}{\sum_{n=1}^{N} \left| \zeta_n^a - \overline{\zeta}_n^a \right|^2 \cdot \sum_{n=1}^{N} \left| \zeta_n^b - \overline{\zeta}_n^b \right|^2}} \tag{8}$$

with $\overline{\zeta}$ denoting the respective mean value of the $N$ samples. For correlation coefficients sufficiently close to 1, the complex-linear regression method can be applied to ascertain whether a systematic error is observed when comparing the two data sets.

[36] On the basis of a least squares method, the complex linear regression searches for the function $f$ that fulfills $\sum_{n=1}^{N} (f(\zeta_n^a) - \zeta_n^b)^2 = min$ and can be described as $f(\zeta^a) = m \cdot \zeta^b + c$ $c$ with $m = |m| \cdot e^{-i \cdot \Psi}$ and $c = |c| \cdot e^{-i \cdot \Theta}$. These describe the amplitude factor $|m|$, the phase correction $\Psi$ and the origin correction $c$ (with amount $|c|$ and direction $\Theta$). A perfect fit of two independent data sets would be characterized by a correlation coefficient and an amplitude factor of value 1 and phase and origin corrections of value 0.

[37] The comparison between the results from TiME extracted from 5′ simulation with the full forcing and the ST103 data set are shown in Table 3. Correlation coefficients range between 0.90 and 0.97 indicating a very good agreement with measurements. Amplitude factors range from 1.0 to 1.4 showing that the model tends to overestimate tidal amplitudes. From data assimilation models we know that the assimilation process compensates deficiencies in the description of the physical processes in the model. These can be characterized by dynamical residuals [*Zahel*, 1995] which have been shown to be to a large extent of dissipative nature and in many cases take large values where bottom topography is not properly resolved due to the relatively coarse spatial resolution of the model [*Zahel et al.*, 2000]. In conclusion, the high amplitude factors of Table 3 indicate that these deficiencies cannot be resolved by the increase of resolution or the application of full forcing. They are more likely related to interactions with other processes in the ocean. Such effects could result from baroclinic processes like the generation of internal tides [*Egbert and Ray*, 2000; *Jayne and St. Laurent*, 2001; *Egbert et al.*, 2004]. Phase correction values range from about −20 to 10 degrees with no visible systematic trend among the listed partial tides. The mean value of −6.45 degrees might indicate that the simulated tides tend to arrive a bit too early.

[38] As TiME utilizes a relatively high resolution, a rough comparison to tide gauges from the Northwestern European Shelf has been performed. Data were taken from a compilation of tide gauge sets (O. B. Andersen, personal communication, 2006). A large number of measurements in this compilation are located at or near the coastline and our 5′-resolution is not high enough to accurately simulate local effects. A closer look at individual stations revealed that some of the results at the coastline agree very well between model and measurements while just as many others strongly diverge. Consequently, we chose to only use measurements with a reasonable distance from the coast for a general comparison of the four main partial tides on the Northwestern European Shelf.

[39] The locations of the resulting 62 tide gauges are indicated in Figure 2 and rms differences and results from the complex-linear regression are listed in Table 4. As absolute amplitudes are higher on the shelf, also the rms differences are higher than in Table 2. Correlation coefficients are still greater than 0.89 for all four partial tides. With the exception of $S_2$, amplitude factors are larger than 1, again indicating the tendency toward overestimation of sea surface elevations. The overestimation of the $M_2$ seems to be less pronounced on the Northwestern European Shelf compared to the results of the global ocean.

[40] The values for the $K_1$ and $O_1$, however, are considerably higher. A closer look at the oscillation system of the diurnal tides in the North Sea (not shown) revealed that our

**Table 3.** Complex-Linear Regression Analysis of TiME Compared With ST103

| Tide | $\mu_{ab}$ | $\lvert m \rvert$ | $\Psi$ | $\lvert c \rvert$ | $\Theta$ |
|---|---|---|---|---|---|
| $2N_2$ | 0.95 | 1.14 | −13.69 | 0.10 | 16.50 |
| $\mu_2$ | 0.93 | 1.04 | −15.02 | 0.17 | 19.20 |
| $N_2$ | 0.97 | 1.32 | −11.44 | 0.55 | 91.55 |
| $\nu_2$ | 0.97 | 1.29 | −8.33 | 0.10 | 104.77 |
| $M_2$ | 0.95 | 1.41 | −5.86 | 2.21 | −170.07 |
| $L_2$ | 0.90 | 1.00 | 10.81 | 0.07 | −85.28 |
| $T_2$ | 0.90 | 1.09 | 5.80 | 0.04 | −48.87 |
| $S_2$ | 0.91 | 1.19 | 0.13 | 1.23 | −2.63 |
| $K_2$ | 0.90 | 1.13 | 6.99 | 0.29 | −1.62 |
| $Q_1$ | 0.90 | 1.17 | −19.88 | 0.16 | −38.12 |
| $O_1$ | 0.95 | 1.40 | −21.71 | 0.42 | −15.10 |
| $P_1$ | 0.97 | 1.06 | −5.05 | 0.17 | 19.67 |
| $K_1$ | 0.96 | 1.04 | −6.56 | 0.65 | 2.41 |
| Mean | 0.94 | 1.18 | −6.45 | 0.47 | −8.28 |

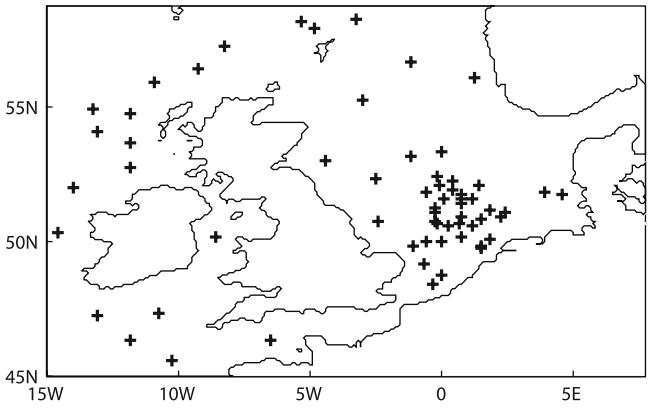


**Figure 2.** Locations of tide gauge measurements on the Northwestern European Shelf.

model predicts an amphidromic point in the inner part of the southern North Sea while other studies suggest a location further north at the Norwegian coast. As a large number of measurements are located in this area, it might explain the large rms values and amplitude factors. The European Shelf is dominated by semi-diurnal tides and, consequently, also the main nonlinearities will be driven by interactions of semi-diurnal tides.

[41] In summary, the high correlation coefficients of Tables 3 and 4 indicate a very good agreement with measurements showing a pronounced tendency toward amplitude overestimation indicated by the amplitude factors. As the $M_2$ tide is also the dominating agent in the generation of nonlinear shallow-water tides, its overestimation by our model should be kept in mind upon further reading.

## 4. Results

[42] The new model TiME describes the complete oscillation system of ocean tides as invoked by the second degree tidal potential. Consequently, this section will only describe a few examples illustrating the basic new aspects being addressed by the approach. Out of the broad frequency band captured by the model, we will first address three major astronomic semi-diurnal and diurnal tides and then focus on a selection of six high-frequency shallow-water tides. The partial tides mentioned in this section are listed in Table 5.

### 4.1. The $M_2$-Tide

[43] As an example, in Figure 3a the principal lunar tide $M_2$ as simulated with the new approach is given. The results compare reasonably well with simulations by other ocean tide models. An interesting result is that the flow direction south of Australia has been simulated in the opposite direction as unconstrained ocean tide had previously predicted [e.g., *Seiler*, 1991]. There, an amphidromic point is described which indicates a westward flow at the Antarctic coast and an eastward flow at the Australian coast. Measurements, however, show that $M_2$ travels westward throughout the entire region between Australia and Antarctica [e.g., *Cartwright et al.*, 1979]. The correction for this inaccuracy was achieved with the first data assimilation models [e.g., *Egbert et al.*, 1994; *Zahel*, 1995].

[44] This effect is now solely achieved by refining the horizontal resolution from 20′ to 5′ (see *Weis* [2006] for details) whereby the amphidromic point between Antarctica and Australia is moving northward with increasing resolution until it finally disappears at the Australian coast. However, this only occurs when the GEBCO bathymetry is used. With the ETOPO bathymetry the amphidromic point remains (not shown). This clearly documents the significant influence of the bottom topography on the simulated oscillation system of ocean tides. Other amphidromic points which change position when assimilating data have not been affected in our simulations, such as the amphidrome in the Pacific part of the Southern Ocean.

[45] In order to investigate the influence the new forcing approach of TiME has on the tidal dynamics, the results of the $M_2$ as extracted from the real-time simulations have been compared to the results of the reference run with the traditional partial tide approach (not shown). Three conclusions can be drawn:

[46] 1. The major parts of the global ocean show differences of less then ±5 cm which first of all documents that the new approach with subsequent harmonic analysis is implemented correctly. The same holds for the differences in phases.

[47] 2. As a tendency, amplitudes have been reduced due to the new forcing approach.

[48] 3. The highest values of up to 50 cm are found along the coastlines, especially in the extended shelf areas, notably along the coasts from Australia all the way to Alaska. Major differences in the Atlantic oceans are found on the Patagonian Shelf, the North Sea and the Hudson Bay.

[49] In order to take a closer look at shelf areas with strongest differences, Figure 3 shows excerpts of the Northwestern European and the Patagonian Shelf which were chosen because of the availability of regional modeling studies and tide gauge measurements [e.g., *Davies et al.*, 1997; *Kwong et al.*, 1997; *Glorioso and Flather*, 1997].

[50] The propagation of the $M_2$ on the European Shelf (Figure 3b) is for the major parts in very good agreement with the results of the three-dimensional regional model of *Kwong et al.* [1997], especially in the North Sea, where amplitudes of up to 2 m and more are calculated by both models. The main difference in the North Sea is the development of a second amphidromic point west of the Danish coast in our results. In the work of *Kwong et al.* [1997], the two amphidromic points shown in Figure 3b are merged to a single one. This leads to a somewhat slower propagation of the $M_2$ along the Dutch and German coasts in our simulations. The amphidromic point in the southernmost North Sea at the entrance to the English Channel is captured by both models.

**Table 4.** Analysis of TiME on the Northwestern European Shelf

| Tide | rms | $\mu_{ab}$ | $\lvert m\rvert$ | $\Psi$ | $\lvert c\rvert$ | $\Theta$ |
|---|---|---|---|---|---|---|
| $M_2$ | 41.08 | 0.89 | 1.24 | 17.43 | 6.56 | −68.44 |
| $S_2$ | 12.79 | 0.91 | 0.90 | 32.49 | 1.92 | 58.31 |
| $K_1$ | 6.84 | 0.94 | 1.51 | −56.10 | 1.60 | 99.34 |
| $O_1$ | 8.54 | 0.92 | 2.24 | −13.97 | 3.18 | −37.33 |

**Table 5.** Partial Tides Discussed in Sections 4 and 5

| Tide | Coefficient $k_{pt}$ | Doodson Number | Argument | | | | | | | Frequency $\sigma_{pt}$ [deg/hour] | Origin[a] |
|---|---|---|---|---|---|---|---|---|---|---|---|
| | | | $t$ | $s$ | $h$ | $p$ | $p_s$ | $N$ | $\phi$ | | |
| $O_1$ | 0.37689 | 145 555 | 1 | −2 | 1 | 0 | 0 | 0 | −90 | 13.943036 | M |
| $K_{1m}$ | 0.36233 | 165 555 | 1 | 0 | 1 | 0 | 0 | 0 | +90 | 15.041069 | M |
| $K_{1s}$ | 0.16817 | 165 555 | 1 | 0 | 1 | 0 | 0 | 0 | +90 | 15.041069 | S |
| $\mu_2$ | 0.02777 | 237 555 | 2 | −4 | 4 | 0 | 0 | 0 | 0 | 27.968208 | M |
| $N_2$ | 0.17387 | 245 655 | 2 | −3 | 2 | 1 | 0 | 0 | 0 | 28.439730 | M |
| $M_2$ | 0.90812 | 255 555 | 2 | −2 | 2 | 0 | 0 | 0 | 0 | 28.984104 | M |
| $S_{2s}$ | 0.42286 | 273 555 | 2 | 0 | 0 | 0 | 0 | 0 | 0 | 30.000000 | S |
| $S_{2m}$ | 0.00072 | 273 555 | 2 | 0 | 0 | 0 | 0 | 0 | 0 | 30.000000 | M |
| $2MS_2$ | – | 237 555 | 2 | −4 | 4 | 0 | 0 | 0 | 0 | 27.968208 | $2 \times M_2 - S_2$ |
| $2SM_2$ | – | 291 555 | 2 | 2 | −2 | 0 | 0 | 0 | 0 | 31.015896 | $2 \times S_2 - M_2$ |
| $MK_3$ | – | 365 555 | 3 | −2 | 3 | 0 | 0 | 0 | −90 | 44.025173 | $M_2 + K_1$ |
| $MN_4$ | – | 445 655 | 4 | −5 | 4 | 1 | 0 | 0 | 0 | 57.423834 | $M_2 + N_2$ |
| $M_4$ | – | 455 555 | 4 | −4 | 4 | 0 | 0 | 0 | 0 | 57.968208 | $2 \times M_2$ |
| $MS_4$ | – | 473 555 | 4 | −2 | 2 | 0 | 0 | 0 | 0 | 58.984104 | $M_2 + S_2$ |
| $M_6$ | – | 655 555 | 6 | −6 | 6 | 0 | 0 | 0 | 0 | 86.952313 | $3 \times M_2$ |

[a]Lunar (M) or solar (S) tidal potential; for shallow-water tides: Combination of astronomic partial tides.

[51] Patterns in the English Channel are also in strikingly good agreement both in amplitudes and phases. Differences can be found in the Irish Sea, where our model only develops a hint at the amphidromic point at the coast of southeast Ireland. Also, Figure 3b indicates wide areas with amplitudes of more than 2 m west of France and the English Channel whereas *Kwong et al.* [1997] calculate amplitudes of about 1.5 m.

[52] The propagation of the $M_2$ on the Patagonian Shelf (Figure 3c) is in excellent agreement with the results of *Glorioso and Flather* [1997] for both amplitudes and phases. Both models calculate an amplitude buildup at the coast in the southern part of more than 3 m. The amphidromic point at 47S latitude is essentially at the same position in both simulations and has the same phase distributions. Both models also develop a second amphidromic point south of the Falkland Islands which lies a bit further east in the chart given by *Glorioso and Flather* [1997].

### 4.2. The $N_2$- and $O_1$-Tide

[53] The propagation of the $N_2$ on the Northwestern European Shelf is similar to the $M_2$, albeit with much lower amplitudes (Figure 3d). Here, the southern North Sea is dominated by only two amphidromic points which closely fit the ones calculated by *Kwong et al.* [1997]. The results also agree well in amplitude and phase values in the North Sea and the English Channel. Again, the amphidromic point in the Irish Sea does not really develop in our simulation and amplitudes in the North Atlantic seem to be overestimated.

[54] With respect to the potential amplitude, the lunar $O_1$ is the strongest tide of the diurnal band. Even though the tides on the Patagonian Shelf are dominated by the semidiurnal constituents, $O_1$ can reach considerable amplitudes of up to 50 cm along the coast (Figure 3e). Comparison with the results of *Glorioso and Flather* [1997] show a general agreement as amplitude and phase distributions and principal propagation patterns are identical. Our simulations show higher amplitudes. The model results differ in the timing of the wave with the Glorioso-model generally leading TiME by some 30 to 50 degrees.

[55] Comparisons of the $N_2$ and $O_1$ to their reference runs (not shown) mainly indicate a reduction of amplitudes in shallow waters comparable to the ones described for the $M_2$. One conspicuous pattern, though, is that the complete forcing also leads to areas of slight amplitude enhancement by up to 2 cm. This is in a way counter-intuitive as the respective astronomical partial tide is losing parts of its energy to a newly generated shallow-water constituent. In order to explain this enhancement, a detailed term balance analysis would be needed which is beyond the scope of this study.

### 4.3. The $M_4$-Tide

[56] The interaction of the $M_2$ with itself leads to the overtide $M_4$ and is the most pronounced shallow-water tide. Figure 4a shows its amplitudes and phases of sea surface elevations on the Northwestern European Shelf as modeled by TiME, as well as the transport ellipses and the energy flux (Figures 4c and 4e). The results are very similar to the ones produced by the FES2004 model [*Lyard et al.*, 2006; *Andersen et al.*, 2006] both in amplitudes and locations of amphidromic points. The models differ in the phase values at various locations, though.

[57] $M_4$ is most pronounced in the English Channel with amplitudes of up to 70 cm and energy fluxes of up to 1000 W $m^{-1}$. There, the tide develops two amphidromic points which are both captured by our model results. Transport ellipses and energy fluxes show that the overtide is generated and increases in strength on its southward propagation along the British east coast. High values also develop in the Irish Sea. Ellipses in the Atlantic part of the figure suggest that a comparatively strong transport is present in the deeper parts of the ocean. However, the energy fluxes indicate that the Northwestern European Shelf is not the primary source for it.

[58] $M_4$ also reaches substantial amplitudes on the Patagonian Shelf with up to 25 cm (Figure 4b). Our results compare well with *Glorioso and Flather* [1997], especially in the amplitudes. The main difference is that, instead of one amphidromic point on the southern Patagonian Shelf, their results suggest another one to the north which is closely linked to it. Similar to the North Sea, the $M_4$ starts being generated at the southernmost coastal part and is rapidly increasing on its northward propagation reaching maximum values at around 50 S (Figures 4d and 4f). This time, the Patagonian Shelf can be identified as a source region for

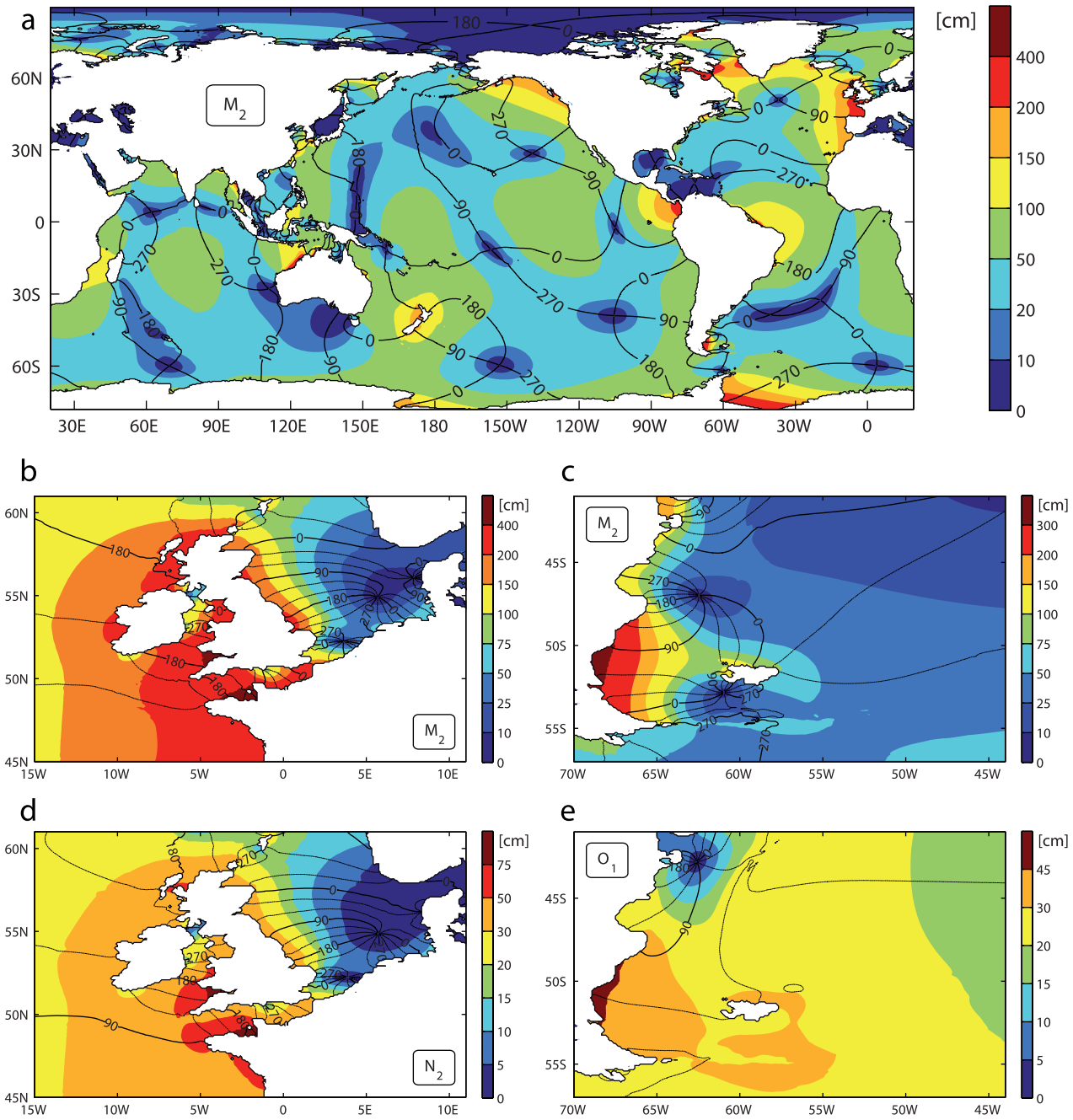


**Figure 3.** (a) Amplitudes and phases of sea surface elevations of $M_2$ and excerpts showing (b) the Northwestern European Shelf, (c) the Patagonian Shelf, (d) the $N_2$ on the Northwestern European Shelf, and (e) the $O_1$ on the Patagonian Shelf.

comparatively high values in deep ocean volume transports and energy fluxes as the $M_4$ propagates northeastward into the Atlantic.

[59] The global propagation of the $M_4$ is shown in Figure 5a as amplitudes and phases of the elevations and in Figure 6a as energy fluxes. Note that amplitudes in all global co-tidal charts of shallow-water tides presented in this paper saturate toward the shelf where they can reach much higher values than indicated by the respective color bar. $M_4$ can reach amplitudes of more than 1 cm in the open ocean, especially in the Atlantic Ocean where also energy fluxes are strongest.

[60] Our results show certain similar patterns in the elevations and energy fluxes from altimeter data as discussed by *Ray* [2007] but differ in just as many others. The strong currents leaving the Patagonian Shelf are in good agreement, as well as the comparatively strong flux from the westernmost tip of South America across the Atlantic in northeasterly direction toward West Africa. Our simulation, however, suggests that this current is in large parts fed by fluxes generated at the east coast of southern Africa. Part of the flux is northward along the African coast and reaches the Gulf of Guinea, but it is not comparable in strength to the one derived from altimetry and it does not form a standing

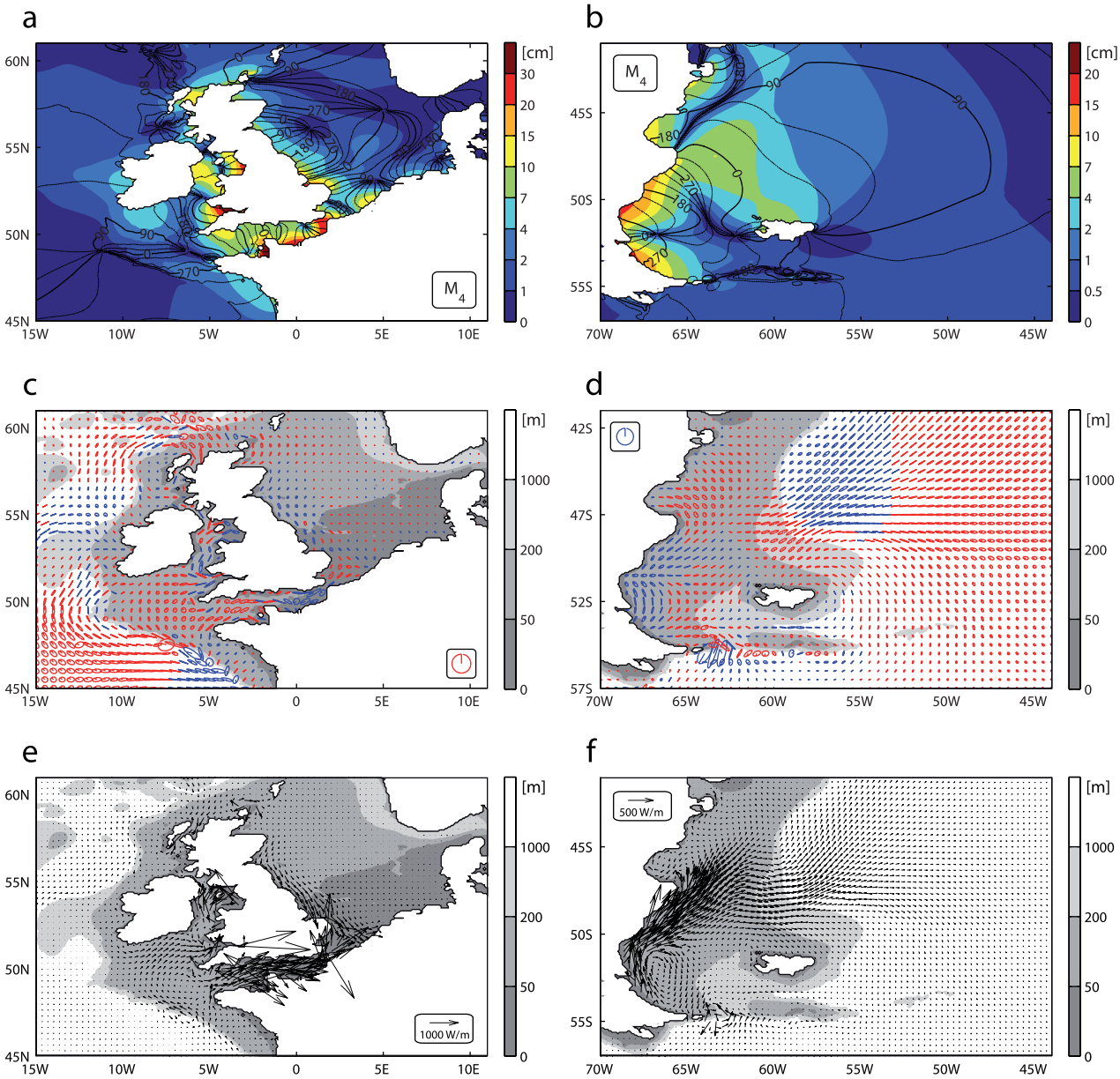


**Figure 4.** Amplitudes and phases of sea surface elevations of $M_4$ on (a) the Northwestern European Shelf and (b) the Patagonian Shelf, (c and d) transport ellipses and (e and f) energy fluxes. A "legend" tidal ellipse has been added. It represents a transport characterized by $U = V = 5\frac{m^2}{s}$ and $\phi_U = 90°$ and $\phi_V = 0°$. Water depths are shown in gray shading. Energy fluxes are calculated as $\mathbf{F} = \frac{1}{2}\,\rho g H \mathbf{v} \zeta \cos \phi_{ev}$ with seawater density $\rho$, and $\phi_{ev}$ indicating the phase differences between elevation and respective velocity component.

wave there and instead moves on in an easterly direction along the coast.

[61] The second conspicuous feature described by *Ray* [2007] of an increase of the $M_4$ on a northward propagation from Northwest-Africa to Europe is not reflected in our results, either. Here, the $M_4$ propagates northwestward into the North Atlantic, a region where the altimetry suggests that the $M_4$ is essentially absent. After reaching the North American continent the $M_4$ propagates back east toward the British Isles.

[62] Although the Atlantic Ocean clearly shows the strongest effect [see *Lyard et al.*, 2006], the $M_4$ of the Southern Pacific Ocean also develops considerably pronounced fluxes with New Zealand as a strong source region and an "S"-shaped propagation through the deep ocean similar to the ones in the Atlantic.

### 4.4. The $MN_4$- and $MS_4$-Tide

[63] Similar to the formation of the $M_4$ as an interaction of the $M_2$ with itself, $M_2 + N_2$ forms the $MN_4$ and $M_2 + S_2$ the $MS_4$ (Figures 5b, 5c, 6b, and 6c). The frequencies of these tides are slightly higher and slightly lower than the one of the $M_4$ (Table 5) and form shallow-water tides with roughly half or a third of the magnitude.

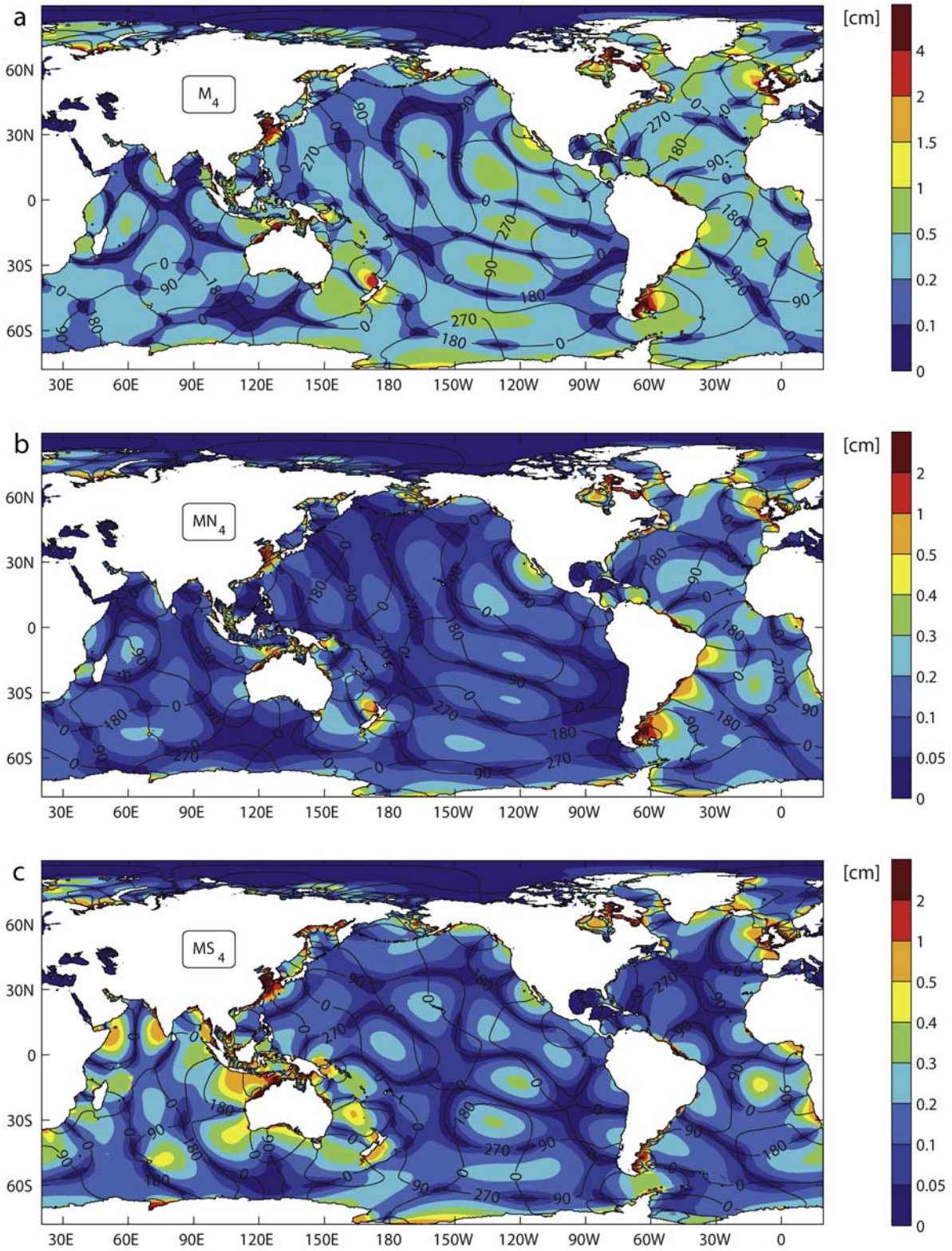


**Figure 5.** Amplitudes and phases of sea surface elevations of (a) $M_4$, (b) $MN_4$, and (c) $MS_4$.

[64] The $MN_4$ describes a propagation similar to $M_4$ with highest elevation amplitudes and strongest energy fluxes in the Atlantic and is generally insignificant in the Indian and Pacific Oceans. The $MS_4$, however, differs substantially from these two in the Atlantic where only in the eastern South Atlantic elevations of higher than 0.5 cm can be found. The $MS_4$ is mainly generated on the Northwestern Australian Shelf where it starts its propagation into the Indian and Pacific Ocean.

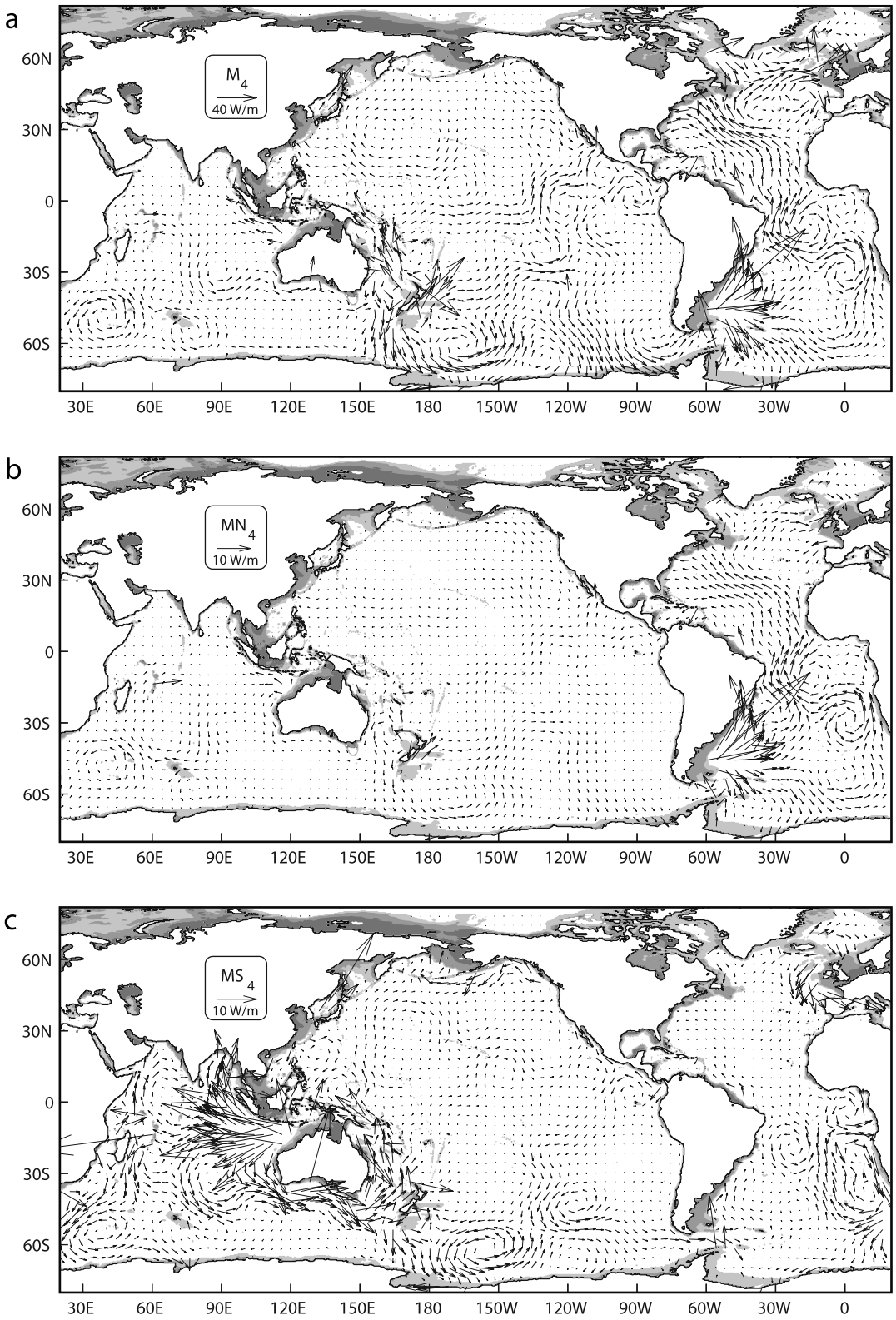


**Figure 6.** Energy fluxes of (a) $M_4$, (b) $MN_4$, and (c) $MS_4$. For graphical reasons, energy flux arrows at water depths shallower than 500 m have been omitted.

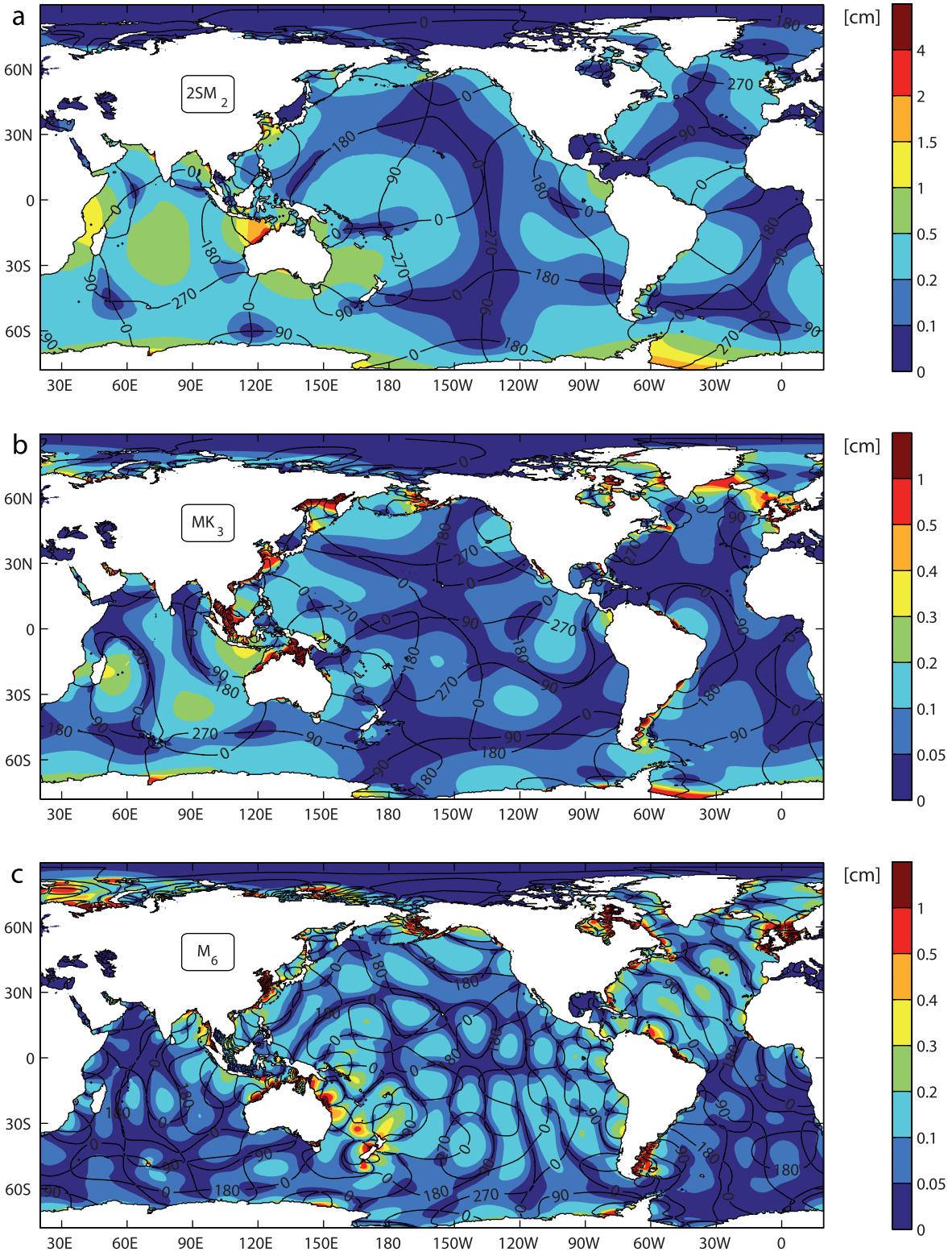


**Figure 7.** Amplitudes and phases of sea surface elevations of (a) $2SM_2$, (b) $MK_3$, and (c) $M_6$.

[65] Parts of this energy flux seem to diverge to the North into the Bay of Bengal which acts as a sink. Another part is turning southward around the Australian continent, travels further south and than back north between Australia and New Zealand.

### 4.5. The $2SM_2$-, $MK_3$-, and $M_6$-Tide

[66] As further examples, we investigate one of the main shallow-water tides from three other tidal bands, the semi-diurnal compound tide $2SM_2$, the terdiurnal $MK_3$ and the sixth-diurnal overtide $M_6$ (Figures 7 and 8).

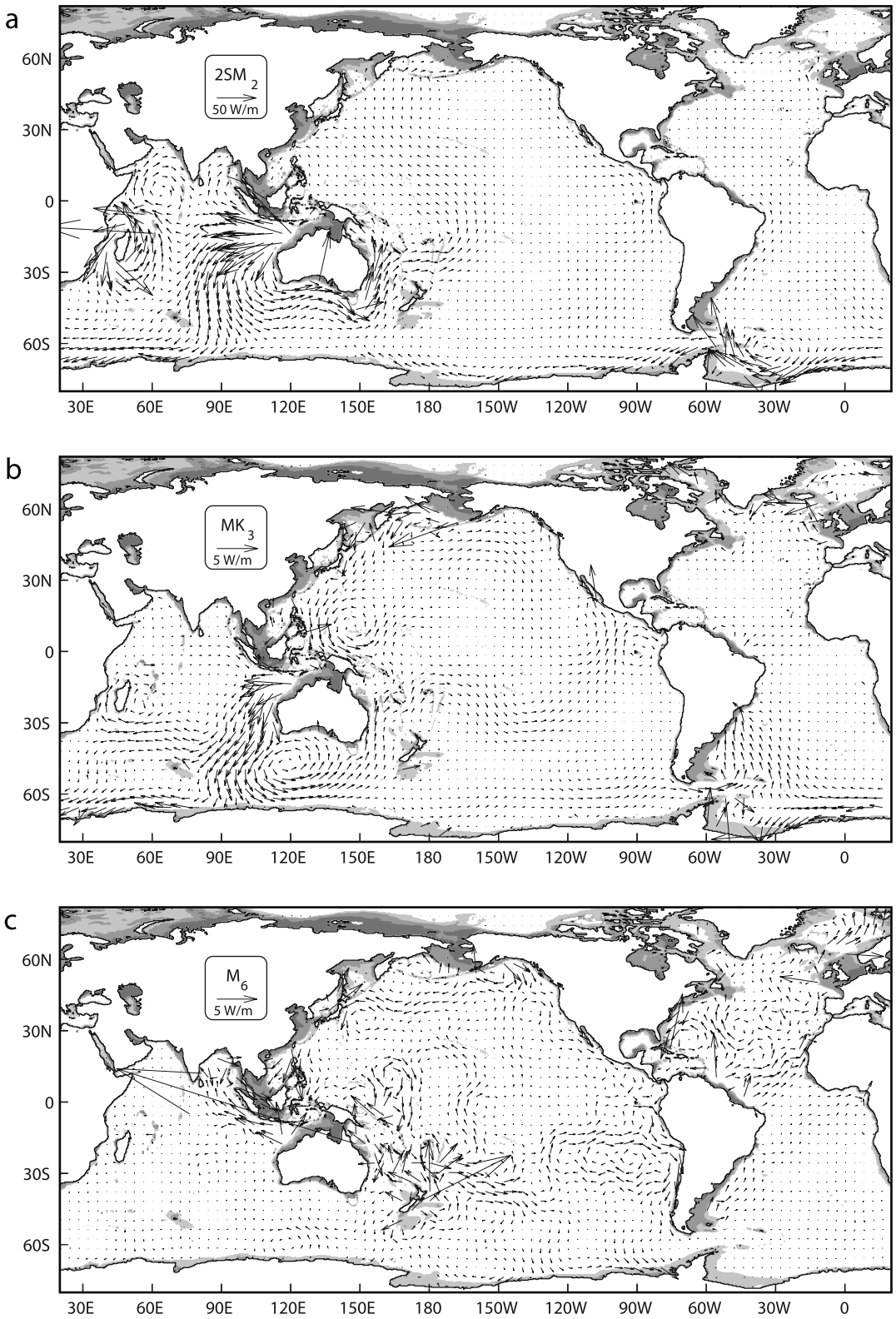


**Figure 8.** Energy fluxes of (a) $2SM_2$, (b) $MK_3$, and (c) $M_6$. For graphical reasons, energy flux arrows at water depths shallower than 500 m have been omitted.

[67] Semi-diurnal compound tides can be obtained by adding two and subtracting one semi-diurnal partial tide. One remarkable feature of this combination is that many will have similar or identical arguments as an astronomical partial tide. For example, the compound tide $2MS_2 = M_2 + M_2 - S_2$ has an identical frequency as the variational lunar tide $\mu_2$ [*Bartels*, 1957]. The harmonic analysis consequently gives the combined effect of $2MS_2$ and $\mu_2$. In a slightly

different combination, though, $S_2 + S_2 - M_2$ results in the semi-diurnal shallow-water tide $2SM_2$ which has no corresponding astronomic counterpart.

[68] Terdiurnals generally form from interaction of a semi-diurnal tide with a diurnal tide, in our case: $M_2 + K_1 = MK_3$. Sixth-diurnal tides result from addition of three semi-diurnals and are mainly generated by the quadratic bottom friction term (equation (3)) in the equation of motion [*Walters and Werner*, 1991]. The strongest tide of this band is the overtide $M_6$.

[69] Of these three, $2SM_2$ is the most significant and is mainly present around the Australian continent and in the Indian Ocean. Like the $MS_4$, most of the $2SM_2$ is formed on the Northwestern Australian Shelf and propagates into the Indian Oceans. The energy flux patterns suggest that one part of the $2SM_2$ again travels around Australia and parts of that flux can still be traced to proceed northward until as far as the Bering Sea. Another part of the energy flux is flowing along Antarctica into the Weddell Sea where it seems to unite with other newly generated $2SM_2$ components. It is also strongly present in an anti-clockwise propagation around Madagascar.

[70] $MK_3$ and $M_6$ are far weaker than $2SM_2$ and barely reach 0.3 cm of elevation amplitudes in deeper waters. Nevertheless they also show coherent energy fluxes in parts of the global oceans. $MK_3$ is also mainly formed on the Northwestern Australian Shelf and shows energy fluxes of a few $W\ m^{-1}$ in the Indian Ocean. After propagating southward and upon hitting Antarctic, the $MK_3$ from the Australian Shelf splits into a eastbound part which can be traced until Southern Mexico and a westbound part which seems to find a sink at the east coast of South America. Another smaller formation site is the Bering Sea from where the $MK_3$ propagates southward into the Pacific.

[71] Propagation of the $M_6$ in the open ocean is even weaker than $MK_3$ barely exceeding 1 W $m^{-1}$. It is mainly present in the region of New Zealand and Eastern Australia, as well as the North Atlantic. Some minor energy fluxes, however, can also be seen in large parts of the Pacific Ocean.

## 5. Conclusions and Discussion

[72] With the novel modeling approach of TiME by forcing a high-resolution ocean tide model with the tidal potential of second degree, a broad frequency band of ocean tides is simulated simultaneously, allowing for interactions of all partial tides involved. With the high horizontal resolution, topographic effects can be captured that can play a significant role even in the open ocean as shown for the $M_2$ amphidromic point south of Australia.

[73] In that respect, TiME as a high-resolution unconstrained time-stepping forward model might for example serve as a reference model for investigations of eigenoscillations of the global ocean [*Platzman et al.*, 1981; *Zahel and Müller*, 2005; *Müller*, 2008] where data assimilation is not possible. It can indicate where an improvement in capturing effects can still be achieved by increasing the resolution.

[74] Nonlinear tidal dynamics have a significant influence on the oscillation system of single partial tides. Results from partial tide forcings have been compared with results of partial tides extracted via harmonic analysis. The most significant differences in both amplitudes and phases are found at the ocean margins, particularly in extended shelf areas where amplitudes are most pronounced and nonlinear effects become important.

[75] These differences can be partly attributed to nonlinear interactions between partial tides, leading to the formation of shallow-water tides. With the novel approach used in TiME global charts of numerically predicted shallow-water tides have been produced. These tides can be captured because: (1) all partial tides are included simultaneously, (2) the model is formulated with nonlinear shallow-water equations, and (3) shelf areas are well represented due to the high spatial resolution.

[76] Shallow-water tides reach amplitudes of up to 70 cm locally. The spatial distribution of volume transports and energy fluxes reveals that the shallow-water tides, after their formation in shallow waters, propagate into the open ocean. Thus shallow-water tides should be regarded after all as a global phenomenon reaching transports of up to 1 $m^2/s$ in the open ocean and energy fluxes of 100 W $m^{-1}$.

[77] Our simulation of the $M_4$ is comparable to the results of several other studies including global and regional modeling as well as results derived from satellite altimetry [*Glorioso and Flather*, 1997; *Kwong et al.*, 1997; *Andersen et al.*, 2006; *Lyard et al.*, 2006; *Ray*, 2007]. We further present global co-tidal charts and energy fluxes for $MN_4$, $MS_4$, $2SM_2$, $MK_3$, and $M_6$ showing that only $2SM_2$ can reach amplitudes comparable to $M_4$. However, all other constituents can also reach considerable elevations in the open ocean. Some of these constituents, like $MS_4$, are hard to derive from satellite altimetry because of their long alias periods [*Andersen et al.*, 2006], others might be considered in the near future.

[78] Our simulations suggest that $M_4$ is not only pronounced in the Atlantic Ocean but can also reach comparatively high amplitudes in the Pacific Ocean, namely around New Zealand. $MN_4$ is mainly found in the Atlantic while $MS_4$, $2SM_2$, and $MK_3$ develop strongest in the Indian Ocean. The overtide $M_6$ reaches only minor amplitudes. However, it is still present far out in the open ocean of the Pacific and North Atlantic.

[79] **Acknowledgments.** We thank Wilfried Zahel and Malte Müller for numerous discussions, the three anonymous reviewers for fruitful comments, and Ulrich Körner and the people at DKRZ for their support on the high-performance computer. This study has been financed by the International Max Planck Research School on Earth System Modelling, Hamburg.

## References

Accad, Y., and C. L. Pekeris (1978), Solution of the tidal equations for the $M_2$ and $S_2$ tides in the world oceans from a knowledge of the tidal potential alone, *Philos. Trans. R. Soc. London, Ser. A*, *290*, 235–266.

Andersen, O. B. (1999), Shallow water tides in the northwest European shelf region from TOPEX/POSEIDON altimetry, *J. Geophys. Res.*, *104*(C4), 7729–7741.

Andersen, O. B., G. D. Egbert, S. Y. Erofeeva, and R. D. Ray (2006), Mapping nonlinear shallow-water tides: A look at the past and future, *Ocean Dyn.*, *56*, 416–429.

Backhaus, J. O. (1983), A semi-implicit scheme for the shallow water equations for application to shelf sea modeling, *Cont. Shelf Res.*, *2*, 243–254.

Backhaus, J. O. (1985), A three-dimensional model for the simulation of the shelf sea dynamics, *Dtsch. Hydrogr. Z.*, *38*, 165–187.

Bartels, J. (1957), Gezeitenkräfte, Handbuch der Physik, Band XLVIII, Geophysik II.

Cartwright, D., B. Zetler, and B. Hamon (1979), Pelagic tidal constants, *IAPSO Publ. Scient.*, *30*, 65.

Davies, A. M., S. C. M. Kwong, and R. A. Flather (1997), Formulation of a variable-function three-dimensional model, with application to the $M_2$ and $M_4$ tide on the Northwest European continental shelf, *Cont. Shelf Res.*, *17*, 165–204.

Egbert, G. D., and R. D. Ray (2000), Significant dissipation of tidal energy in the deep ocean inferred from satellite altimeter data, *Nature*, *405*, 775–778.

Egbert, G. D., A. F. Bennett, and M. G. G. Foreman (1994), TOPEX/POSEIDON tides estimated using a global inverse model, *J. Geophys. Res.*, *99*(C12), 24,821–24,852.

Egbert, G. D., R. D. Ray, and B. G. Bills (2004), Numerical modeling of the global semidiurnal tide in the present day and in the last glacial maximum, *J. Geophys. Res.*, *109*, C03003, doi:10.1029/2003JC001973.

Emery, W. J., and R. E. Thompson (1998), *Data Analysis Methods in Physical Oceanography*, 634 pp., Pergamon Press, Amsterdam.

Foreman, M. G. G., and R. F. Henry (1989), The harmonic analysis of tidal model time series, *Adv. Water Resour.*, *12*, 109–120.

Glorioso, P. D., and R. A. Flather (1997), The Patagonian Shelf tides, *Prog. Oceanogr.*, *40*, 263–283.

Hellmich, A. M. (2003), Ein rechenökonomisches Modul für ephemeridische Gezeitensimulationen, diploma thesis, TU Dresden.

Horn, W. (1967), *Tafeln der Astronomischen Argumente* $V_0 + v$ *und der Korrektionen* $j$,$v$, Deutsches Hydrographisches Institut, Hamburg, Germany.

Hufschmidt, A. (1995), Berechnung des Auflast- und Eigenanziehungspotentials in einem globalen Gezeitenmodell und Auswirkungen auf die Energiebilanz, diploma thesis, Univ. of Hamburg.

IOC, IHO and BODC (2003), Centenary Edition of the GEBCO Digital Atlas, published on CD-ROM on behalf of the Intergovernmental Oceanographic Commission and the International Hydrographic Organization as part of the General Bathymetric Chart of the Oceans, British Oceanographic Data Centre, Liverpool, U.K.

Jayne, S. R., and L. C. St. Laurent (2001), Parameterizing tidal dissipation over rough topography, *Geophys. Res. Lett.*, *28*(5), 811–814.

Kwong, S. C. M., A. M. Davies, and R. A. Flather (1997), A three-dimensional model of the principal tides on the European Shelf, *Prog. Oceanogr.*, *39*, 205–262.

Lefèvre, F., F. H. Lyard, C. Le Provost, and E. J. O. Schrama (2002), FES99: A global tide finite element solution assimilating tide gauge and altimetric information, *J. Atmos. Oceanic Technol.*, *19*, 1345–1356.

Le Provost, C. (1991), Generation of overtides and compound tides, in *Tidal Hydrodynamics*, edited by B.B. Parker, pp. 269–295, Wiley, New York.

Le Provost, C. (1995), A new sea truth data set for tides, available at ftp://meolipc.img.fr/pub/ST103.

Lyard, F., F. Lefevre, T. Letellier, and O. Francis (2006), Modelling the global ocean tides: Modern insights from FES2004, *Ocean. Dyn.*, *56*, 394–415.

Müller, M. (2008), Synthesis of forced oscillations. part I: Tidal dynamics and the influence of the loading and self-attraction effect, *Ocean Modell.*, *20*, 207–222.

NOAA (1988), Data Announcement 88-MGG-02, Digital relief of the Surface of the Earth, NOAA, Natl. Geophys. Data Cent., Boulder, Colo.

Parke, M. E. (1982), $O_1$, $P_1$, $N_2$ models of the global ocean tide on an elastic earth plus surface potential and spherical harmonic decompositions for $M_2$, $S_2$ and $K_1$, *Mar. Geod.*, *6*, 35–81.

Parker, B. B. (1991), The relative importance of the various nonlinear mechanisms in a wide range of tidal interactions, in *Tidal Hydrodynamics*, edited by B. B. Parker, pp. 237–268, Wiley, New York.

Platzman, G. W., G. A. Curtis, K. S. Hansen, and R. D. Slater (1981), Normal modes of the world ocean. part 2: Description of modes in the range 8 to 80 hours, *J. Phys. Oceanogr.*, *11*, 579–603.

Pugh, D. T. (1987), *Tides, Surges and Mean Sea-Level: A Handbook for Engineers and Scientists*, 472 pp., Wiley, Chichester, U.K.

Ray, R. D. (2007), Propagation of the overtide $M_4$ through the deep Atlantic Ocean, *Geophys. Res. Lett.*, *34*, L21602, doi:10.1029/2007GL031618.

Seiler, U. (1989), An investigation to the tides of the world ocean and their instantaneous angular momentum budgets, *Mitt Inst. Meereskd. Univ. Hambg.*, *29*, 101.

Seiler, U. (1991), Periodic changes of the angular momentum budget due to the tides of the world ocean, *J. Geophys. Res.*, *96*(B6), 10,287–10,300.

Shum, C. K., et al. (1997), Accuracy assessment of recent ocean tide models, *J. Geophys. Res.*, *102*(C11), 25,173–25,194.

Thomas, M., and J. Sündermann (1999), Tides and tidal torques of the world ocean since the last glacial maximum, *J. Geophys. Res.*, *104*(C2), 3159–3183.

Thomas, M. (2001), Ozeanisch induzierte Erdrotationsschwankungen—Ergebnisse eines Simultanmodells für Zirkulation und ephemeridische Gezeiten im Weltozean, Ph.D. thesis, Univ. of Hamburg, 129 pp.

Thomas, M., J. Sündermann, and E. Maier-Reimer (2001), Consideration of ocean tides in an OGCM, and impacts on subseasonal to decadal polar motion excitation, *Geophys. Res. Lett.*, *28*(12), 2457–2460.

Walters, R. A., and F. E. Werner (1991), Nonlinear generation of overtides, compound tides, and residuals, in *Tidal Hydrodynamics*, edited by B. B. Parker, pp. 297–320, Wiley, New York.

Weis, P. (2006), Ocean tides and the Earth's rotation—Results of a high-resolving ocean model forced by the lunisolar tidal potential, in *Reports on Earth System Science*, vol. 36, 111 pp., Max Planck Institute of Meteorology, Hamburg.

Zahel, W. (1977), A global hydrodynamic-numerical 1°-model of the ocean-tides; the oscillation system of the $M_2$-tide and its distribution of energy dissipation, *Ann. Geophys.*, *33*, 31–40.

Zahel, W. (1995), Assimilating ocean tide determined data into global tidal models, *J. Mar. Syst.*, *94*(6), 3–13.

Zahel, W., and M. Müller (2005), The computation of the free barotropic oscillations of a global ocean model including friction and loading effects, *Ocean. Dyn.*, *55*, 137–161.

Zahel, W., J. H. Gaviño, and U. Seiler (2000), Balances de Energía y Momento Angular de un Modelo Global de Mareas con Asimilacíon de Datos, *Geos*, *20*(4), 400–413.

J. Sündermann, Institute of Oceanography, University of Hamburg, Bundesstrasse 53, D-20146 Hamburg, Germany.

M. Thomas, Geodesy and Remote Sensing, GeoForschungsZentrum, Telegrafenberg, D-14473 Potsdam, Germany.

P. Weis, Institute of Isotope Geochemistry and Mineral Resources, ETH Zurich, Clausiusstrasse 25 (NW), CH-8092 Zurich, Switzerland. (philipp.weis@erdw.ethz.ch)